



## Detection of lead content in oilseed rape leaves and roots based on deep transfer learning and hyperspectral imaging technology

Xin Zhou<sup>a,\*</sup>, Chunjiang Zhao<sup>a,b,c</sup>, Jun Sun<sup>a,1</sup>, Kunshan Yao<sup>a</sup>, Min Xu<sup>a</sup>

<sup>a</sup> School of Electrical and Information Engineering of Jiangsu University, Zhenjiang 212013, China

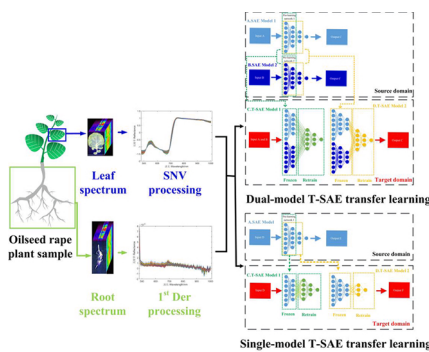
<sup>b</sup> National Engineering Research Center for Information Technology in Agriculture, Beijing 100097, China

<sup>c</sup> National Engineering Laboratory for Agri-product Quality Traceability, Beijing 100097, China

### HIGHLIGHTS

- T-SAE models were proposed to transfer deep learning models.
- Make full use of the hyperspectral information of oilseed rape leaves and roots.
- Hyperspectral imaging applied to forecast lead stress level of oilseed rape plants.
- The established T-SAE models achieve high-precision prediction of Pb concentration.

### GRAPHICAL ABSTRACT



### ARTICLE INFO

**Keywords:**  
Hyperspectral image  
Deep learning  
Transfer learning  
Oilseed rape  
Heavy metal

### ABSTRACT

The evaluation capability of hyperspectral imaging technology was studied for the forecasts of heavy metal lead concentration of oilseed rape plant. In addition, a transfer stacked auto-encoder (T-SAE) algorithm including two network methods, the dual-model T-SAE and the single-model T-SAE, was proposed in this paper. The hyperspectral images of oilseed rape leaf and root were acquired under different Pb stress concentrations. The entire region of the oilseed rape leaf (or root) was selected as the region of interest (ROI) to extract the spectral data, and standard normalized variable (SNV), first derivative (1<sup>st</sup> Der) and second derivative (2<sup>nd</sup> Der) were used to preprocess the ROI spectra. Besides, the principal component analysis (PCA) algorithm was used to reduce the dimensionality of the spectral data before and after preprocessing. Hence, the best pre-processed data was determined for subsequent research and analysis. Furthermore, the SAE deep learning networks were built based on the oilseed rape leaf data, oilseed rape root data, and the combined data of oilseed rape leaf and root based on the best pre-processed spectral data. Finally, the T-SAE models were obtained through transfer learning of the best SAE deep learning network. The results show that the best preprocessing algorithms of the oilseed rape leaf and root spectra were SNV and 1<sup>st</sup> Der algorithm, respectively. In addition, the prediction set recognition accuracy of the best T-SAE model of Pb stress gradient in oilseed rape plants was 98.75%. Additionally, the prediction set coefficient of determination of the best T-SAE model of the Pb content in the oilseed rape leaf and root

\* Corresponding author.

E-mail addresses: [862218958@qq.com](mailto:862218958@qq.com) (X. Zhou), [sun2000jun@sina.com](mailto:sun2000jun@sina.com) (J. Sun).

<sup>1</sup> Co-corresponding author.



data were 0.9215 and 0.9349, respectively. Therefore, a deep transfer learning method combined with hyperspectral imaging technology can effectively realize the qualitative and quantitative detection of heavy metal Pb in oilseed rape plants.

## 1. Introduction

A soil environment contaminated by toxic metals is unsuitable for modern agricultural production, because toxic metals have a cumulative effect in crops and can cause harm to human health through the food chain [11]. In 2014, the Ministry of Environmental Protection and the Ministry of Land and Resources of China jointly issued their “Report on the Status of Soil Pollution in China”, and conducted a national soil survey from 2005 to 2013, covering more than 70% of China’s land area [37]. The survey report pointed out that 19% of agricultural soil was polluted by inorganic and (or) organic pollutants, and 82.4% of the pollution was caused by metals and metalloids. Among the soils considered to be polluted, the percentage of measurements exceeding the authorized Pb concentration limit is 1.5% [23,21]. Lead (Pb) is a highly hazardous toxic metal that can hinder hematopoiesis, alter immune and sensory functions, and affect the cardiovascular, kidney, digestive, reproductive and nervous systems [2]. Oilseed rape is one of the most important oil crops in China, and its total output ranks first in the world [1]. The cultivation and distribution of oilseed rape in China are mainly concentrated in Southern and Northern China, and this distribution overlaps with the toxic metal Pb pollution area [13]. Therefore, it is of great significance to classify the environmental lead stress concentration and detect the concentration of heavy metal lead of oilseed rape plants.

Hyperspectral imaging (HSI) technology is a non-destructive testing technology that integrates spectrum and image [25,40]. At present, some research progress has been made in the analysis of crop and soil hyperspectral image information under the toxic metal environment. Some studies have derived parameters from spectral variations associated with heavy metal Pb, mercury (Hg) and chromium (Cr) in soil and to explore the possibility of extending the use of these parameters to hyperspectral images [33,12]. Besides, airborne hyperspectral imaging is used to estimate the concentration of heavy metals in the soil, and the determination coefficient  $R^2$  value of the best random forest (RF) model is 0.74 for the determination of Pb content in soil [27]. In addition, lab- and airborne HSI technology is used to locate areas contaminated by heavy metals, the results suggest that hyperspectral scanning can spectrally discriminate samples from a mineralized zone, and the lab-based hyperspectral data outcompetes the airborne hyperspectral data for vegetation in identifying areas of potential regional heavy metal pollution [5]. The deep learning (DL) algorithm has a multi-layer neural network structure, which can handle extremely large-scale data, and significantly improves the modeling performance in many spectral analysis tasks [43]. In recent years, scholars have successfully applied deep learning to a dimensionality reduction of the hyperspectral information [29,9], e.g. HSI technology combined with DL methods to classify the soil contaminated by Cr [30], predict the heavy metal cadmium (Cd) and Pb content in lettuce leaves [40] and detect heavy metal zinc (Zn) in optically inactive inland water [19]. However, when the detection target is the same but the input data differ, it is often necessary to apply retraining to obtain a new deep learning model, and it is impossible to make full use of the deep learning model studied by previous researchers [8,35].

Transfer learning (TL) is a new learning paradigm in machine learning, and it is used in the general transfer of information between different domains [20]. A stacked auto-encoder is a more common deep learning algorithm, which mainly merges low-level features (from the initial input layers) into higher-level abstractions (the last deep feature layer) to achieve the target detection [24]. Hence, the main aim of TL is to use the already acquired knowledge to avoid the expensive task of

training large DL models from scratch [18]. To the best of our knowledge, no research has explored the study of deep transfer learning (DTL) combined with hyperspectral images to classify the environmental lead stress concentration and detect lead concentration of oilseed rape plants.

The main aims of this paper are: (1) to examine the feasibility of using hyperspectral imaging technology to classify Pb stress concentration and detect lead concentration of oilseed rape plants; (2) to determine the best pre-processed spectral data for subsequent research and analysis, (3) to explore the reliability of the qualitative and quantitative detection of heavy metal lead in oilseed rape plants based on the hyperspectral depth features and (4) to explore the feasibility of improving the accuracy of the Pb qualitative and quantitative detection through deep transfer learning models.

## 2. Materials and methods

### 2.1. Planting materials and growth environments

The experimental growth conditions were based on previous research with some modifications [4]. The surfaces of the oilseed rape seeds (Qinyou No. 10, hybrid rape) were first surface-disinfected with 70% ethanol, and the seeds were then germinated in deionized water in petri dishes at 25 °C for 4 days in the darkness. After germination, the seedlings were moved to a perlite solid substrate for cultivation. After 10 days of growth, the seedlings were fully watered with a Hoagland nutrient solution (pH = 6.0) that fully penetrates the transplanting substrate, which was carried out twice a day. Following 30 days of oilseed rape growth, the seedlings were watered for 12 days with a Hoagland nutrient solution (pH = 6.0) added with heavy metal lead (Pb) reagents, and the concentrations of which (·) were 0, 50, 100, 200 and 300 µM, respectively. Finally, 250 oilseed rape plants were cultivated and divided into 5 groups, with 50 plants in each group. When the number of leaves of oilseed rape leaves reached 10–12 pieces after 30 days of growth, the leaves at the 8th leaf position and the whole oilseed rape roots were selected as samples and placed in different label bags for hyperspectral image information collection. Finally, the total number of samples collected from the oilseed rape plants totaled 500, including 250 oilseed rape leaves and 250 oilseed rape roots.

### 2.2. Hyperspectral imaging acquisition and calibration

Visible-near infrared (Vis-NIR) hyperspectral images were obtained through a Vis-NIR hyperspectral imaging acquisition device covering the spectral range of 400.68–1001.61 nm with a spectral resolution of 2.8 nm using the following collection devices: a spectrograph (ImSpectorV10, Spectral Imaging Ltd., Oulu, Finland), a sCMOS camera (Zyla 4.2 Plus, Andor Technology, Inc., UK), a standard C-mount zoom lens (F/2.4, f = 23 mm, OLE23, Specim Ltd., Finland), a 150 W quartz tungsten-halogen light source (3900-ER, Illumination Technology, Inc., USA), a stepper motor(MSI300, Isuzu Optics Corp., Taiwan, China) and the dark cover (DC1300, Isuzu Optics Corp., Taiwan, China). Moreover, the hyperspectral image acquisition device was a push-broom system. There were 411 spectral channels ranging from 480.46 nm to 1001.61 nm with a spectral resolution of 2.8 nm. To reduce the influence of environment factors and improve the signal-to-noise ratio (SNR), the acquired hyperspectral image  $I_o$  was further corrected using the following equation [40]:

$$I_c = \frac{I_o/E_o - D/E_d}{W/E_w - D/E_d} \times 100 \quad (1)$$

**Table 1**

Actual detection values of Pb in rape leaves and roots after chemical detection.

H ( $\mu\text{M}$ )	Pb concentration in oilseed rape leaves			Pb concentration in oilseed rape roots		
	Min (mg/kg)	Max (mg/kg)	Mean (mg/kg)	Min (mg/kg)	Max (mg/kg)	Mean (mg/kg)
0	0.0000	0.0000	0.0000	0.0000	0.0000	0.0000
50	0.06081	0.09633	0.08667	0.9683	0.1403	0.1293
100	0.09854	0.1163	0.1002	0.1690	0.1931	0.1804
200	0.1196	0.1421	0.1279	0.1945	0.2097	0.1969
300	0.1559	0.1893	0.1692	0.2074	0.2499	0.2246

Note: H represents the Pb stress concentration of rape plants. Min, Max and Mean represent the minimum, maximum and average values of Pb content in oilseed rape leaf (or root) samples, respectively.

where  $I_c$  is the corrected hyperspectral image expressed as the relative reflectance (%),  $I_o$  is the original acquired hyperspectral image,  $D$  is a dark image (with approximately 0% reflectance) recorded by closing completely the aperture of the camera, and  $W$  is the white reference image obtained using a white calibration tile (Specim Ltd., Finland) with a uniform, stable and high reflectance standard (with approximately 99% reflectance). In addition,  $E_o$ ,  $E_d$  and  $E_w$  are the CCD camera exposure time settings for the samples, whiteboard reference (Ref-white), darkboard reference (Ref-dark), respectively.

In this experiment, the distance between the CCD camera lens and the oilseed rape, the CCD camera exposure times of the black and white boards and samples, and the moving speed of the sample stage were 0.45 m, 7 ms, 7 ms, 14 ms and 4.1848 mm/s, respectively.

### 2.3. Chemical testing

After obtaining the hyperspectral image, the leaves and roots of the oilseed rape were washed three times with deionized water. These samples were ground into powder after drying under a temperature of 120 °C until reaching a constant weight. To effectively detect the Pb contents in oilseed rape leaves and roots, 0.02 g of the dried sample powder was weighed and digested, and then the total Pb content of the sample was then determined using a atomic absorption spectrometer (ZEEenit®700P, Analytik Jena AG, Germany). The results of the Pb content measured in the oilseed rape leaf and root samples are shown in Table 1. As Table 1 indicates, there were differences in the residual values of the actual Pb content residual values in the oilseed rape leaf (or root) samples under different Pb stress concentrations. This provided an important reference in the present study to determine the category of Pb stress based on the oilseed rape leaf and root hyperspectral data.

### 2.4. Spectrum acquisition and preprocessing

Each hyperspectral image information contained not only the leaf (or root) information of oilseed rape, but also the background information. To effectively avoid background interference, the entire region of the oilseed rape leaf (or root) was selected as the region of interest (ROI) to extract the hyperspectral data (Fig. 1). It can be seen from Fig. 1 that the ratio method was used to obtain the mask images of oilseed rape leaf and root and thereby realize the image segmentation between the oilseed rape leaf (or root) and background. Defining the image after ratio processing as  $F(X,Y)$ , find a suitable gray value  $t$  in  $F(X,Y)$  is found according to certain criteria, and a mask image  $G(X,Y)$  can then be

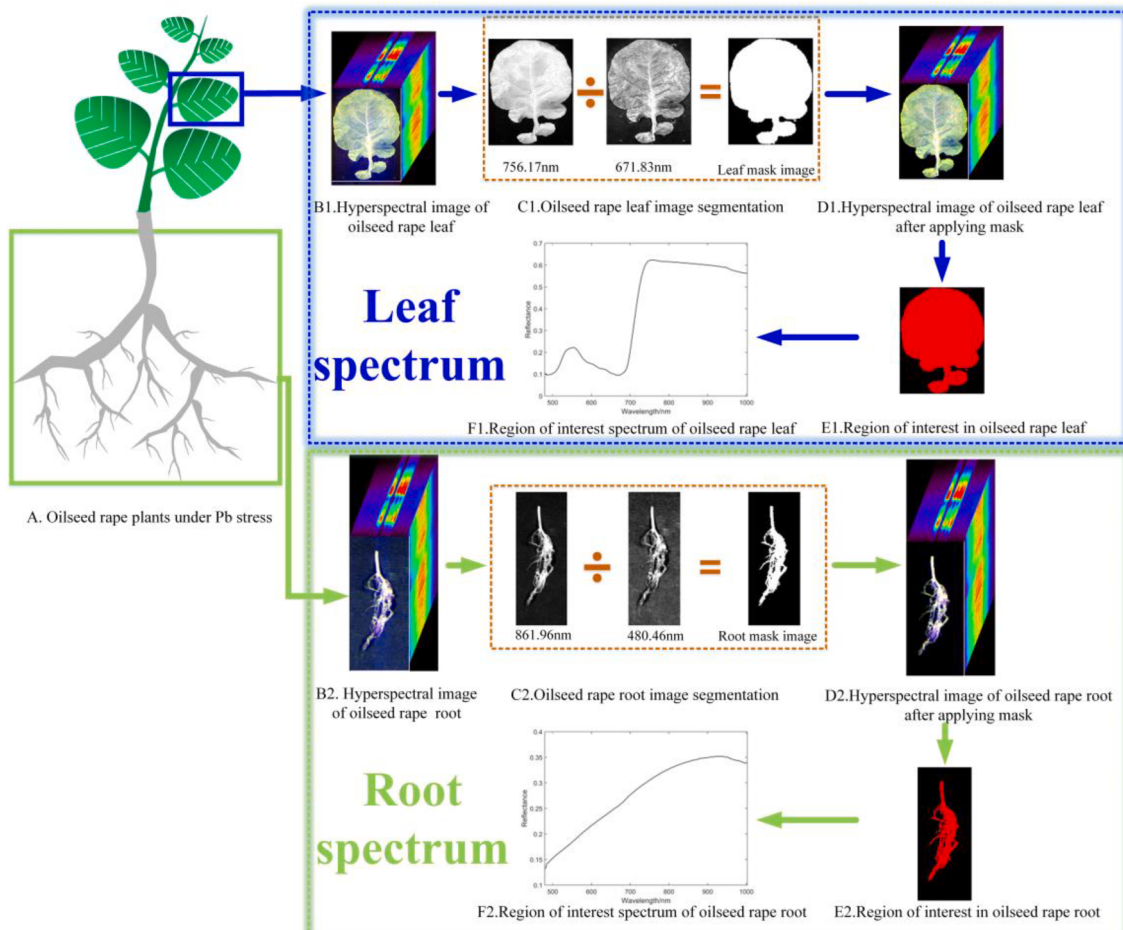


**Fig. 1.** The process of obtaining the ROI spectra of oilseed rape leaf and root.

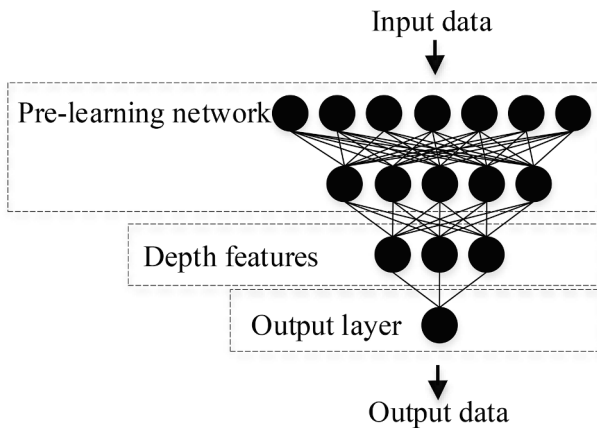


**Fig. 2.** The SAE structure diagram of 4-layer network.

calculated through the following formula:

$$G(X, Y) = \begin{cases} 0 & F(X, Y) \geq t \\ 1 & F(X, Y) < t \end{cases} \quad (2)$$

where the segmentation threshold  $t$  of the oilseed rape leaf and root are 1.3 and 1.6 respectively.

The hyperspectral images information of the oilseed rape leaf and

root were then obtained after applying the mask images. The whole oilseed rape leaf and root regions were selected as the region of interest (ROI) for each sample (oilseed rape leaf or root), and the average spectrum of each ROI was considered as the sample spectrum for subsequent research under the ENVI 4.5 software (Exelis Visual Information Solutions, USA) environment.

Three spectral data preprocessing algorithms were used to process the raw spectral data and evaluate the reliability of the modeled data including the standard normalized variable (SNV) [17], first derivative (1st Der) [31] and second derivative (2nd Der) [3]. By comparing the accuracy of the Pb stress concentration classification model established based on the pre-processed spectral data, the best pre-processed data were determined for subsequent research and analysis. All spectral preprocessing algorithms were implemented using the Unscrambler X 10.4 software (CAMO Technologies Inc., Woodbridge, New Jersey).

## 2.5. Spectral data dimensionality reduction

### 2.5.1. PCA algorithm

A principal component analysis (PCA) is one of the most widely used unsupervised methods in a multivariate analysis [16]. As the main virtue of a PCA, it can significantly reduce the dimension of the spectral data set while discarding relatively little information [14]. To this end, a PCA was used as an exploratory technique to reduce the high dimensionality of the spectral data to a small number of principal component (PC)

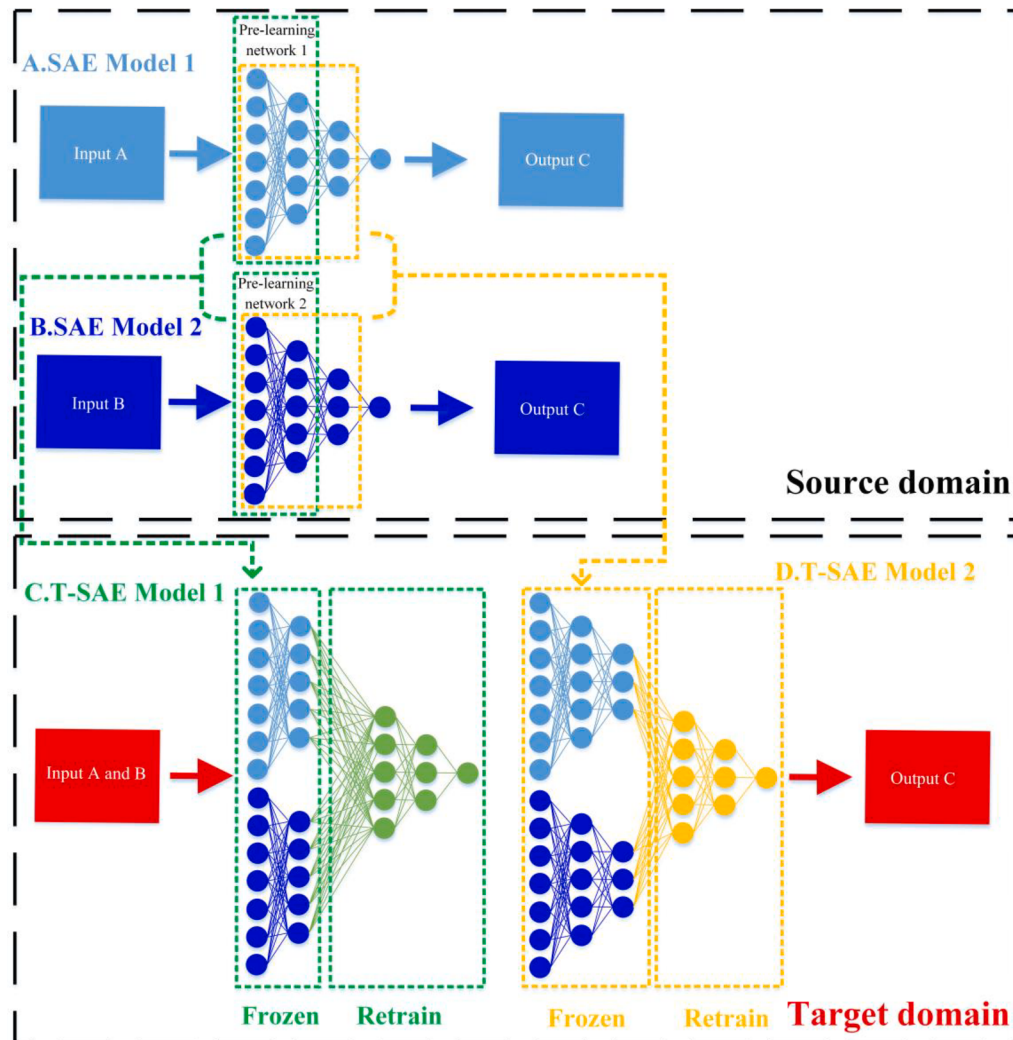


**Fig. 3.** The dual-model T-SAE transfer network structure diagram.

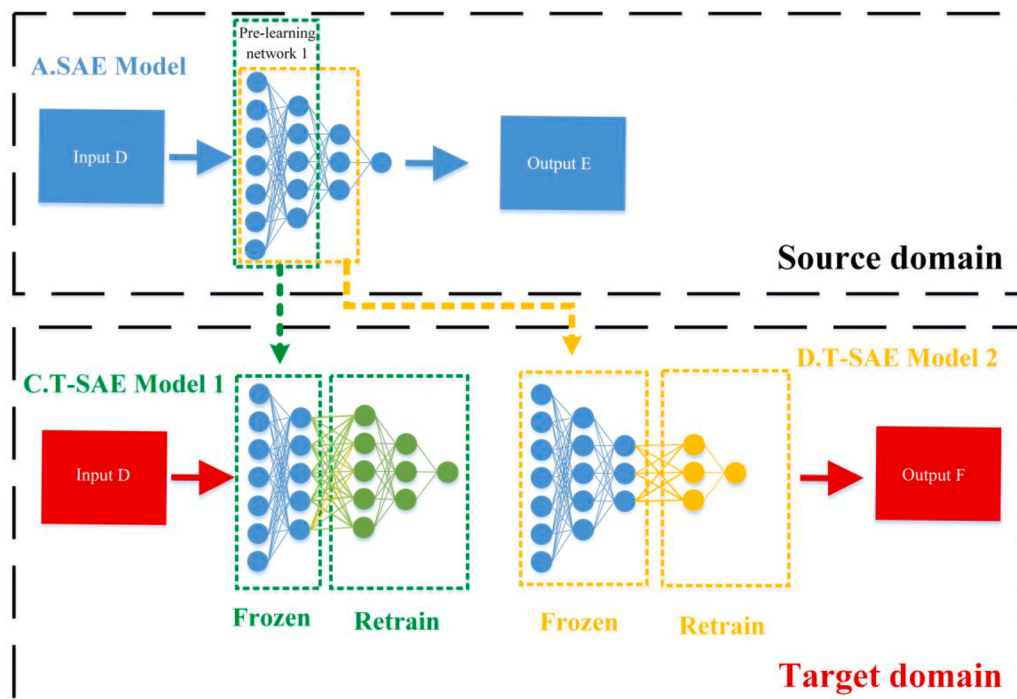


Fig. 4. The single-model T-SAE transfer network structure diagram.

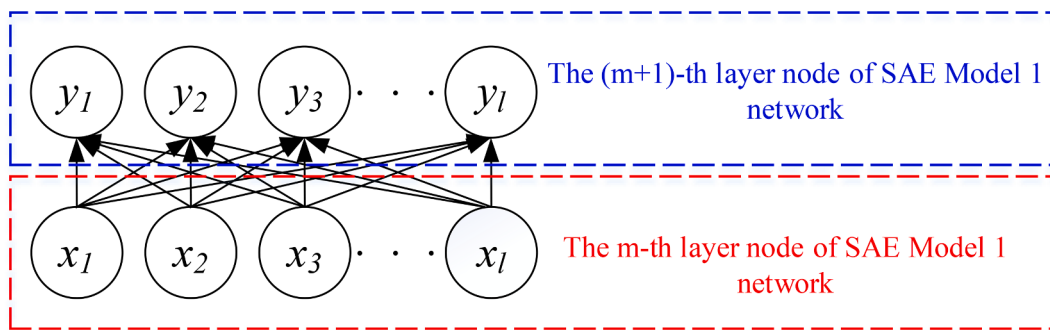


Fig. 5. Extension of transfer SAE model network from layer  $m$  to layer  $m + 1$ .

scores and thereby capture the largest changes in the spectral data. Besides, the PCA dimensionality reduced data were used to classify and detect different concentrations of Pb stress in rape plants. In this paper, the components are retained by PCA dimensionality reduction instead of returning to the wavelength domain, and the retained component score is the cumulative contribution rate greater than or equal to 99.999%. The PCA was executed using Matlab 2014a (The Math Works, Natick, USA).

#### 2.5.2. SAE algorithm

An stacked auto-encoder (SAE) is a deep neural network superimposed from a simple auto-encoder (AE) structure. The depth feature reduction extraction of the SAE is essentially an encoding process, which maps a input training samples nonlinearly into hidden layers through a mapping functions [41]. Besides, the mathematical expression of the relationship is summarized as follows [35]:

$$y = f(x) = s_f(W \times s + b) \quad (3)$$

where  $y$  is the hidden layer presentation,  $s_f$  denotes the activation function,  $W$  is the input-to-hidden weight matrix of the encoding, and  $b$  denotes the bias of the encoding.

Taking the SAE structure of the 4-layer network as an example

(Fig. 2), it can be seen from that the last single node is defined as the output layer network, the third layer was the depth feature extracted by SAE, and the network before the learned depth feature layer was defined as the pre-learning network in this paper. The SAE was implemented in an AE variant framework, which is a Matlab library for developing deep learning models and can use the GPU to speed up the calculations (available at [https://github.com/zheng-yuwei/Stacked\\_Autoencoder](https://github.com/zheng-yuwei/Stacked_Autoencoder)).

#### 2.5.3. T-SAE Algorithm

In some studies, we would like to further study the deep network relationship model of A (the hyperspectral information of oilseed rape leaves), B (the hyperspectral information of oilseed rape roots) and C (the Pb stress concentration of oilseed rape plants) by completing the deep network relationship models of A and C, and B and C. Assuming that the SAE Model 1 of A and C, and the SAE Model 2 of B and C are established within the source domain, the transfer SAE (T-SAE) framework algorithm based on transfer learning is proposed to build a dual-model transfer network structure for A, B and C (target domains) in this paper (Fig. 3). In addition, We would like to study the deep network relationship model of D (the oilseed rape plant hyperspectral information), E (the environmental lead stress concentration of the oilseed rape plant) and F (the heavy metal lead content of the oilseed rape plant) by

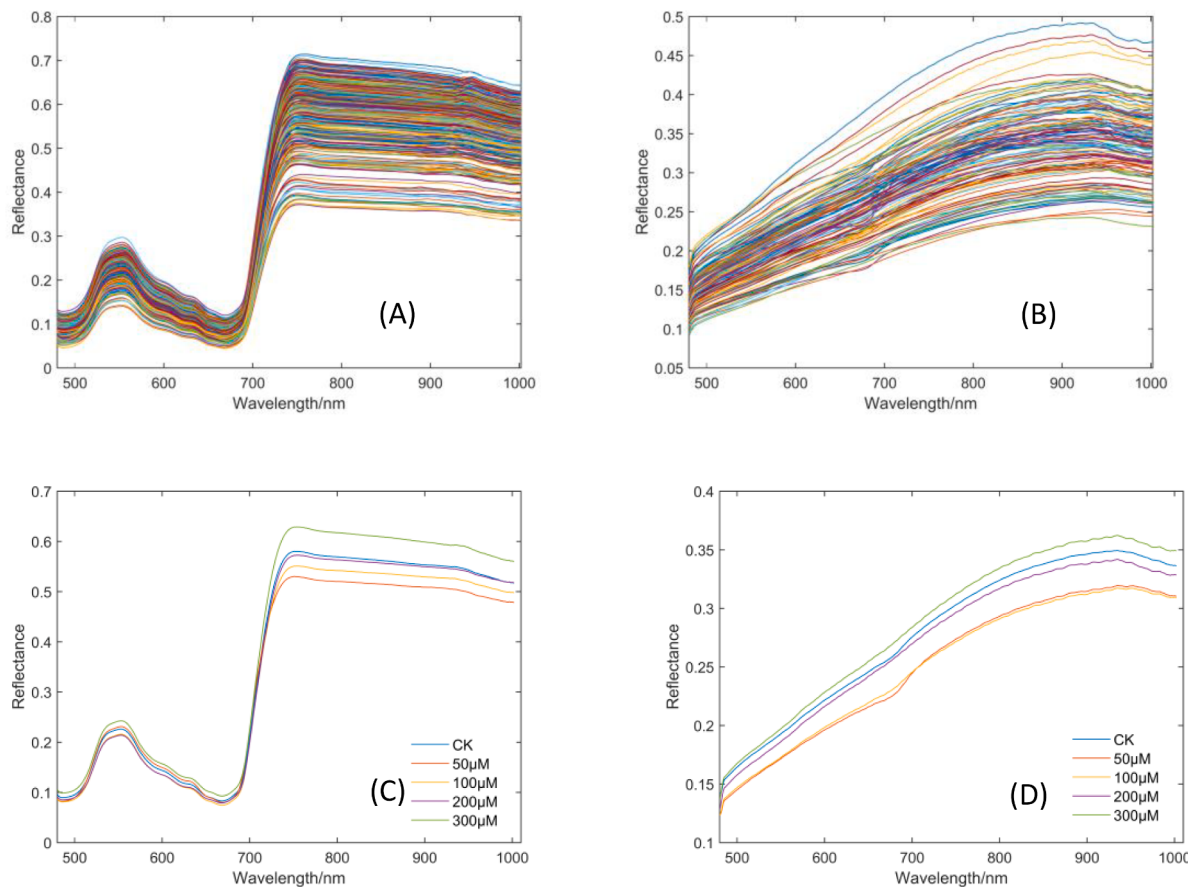


**Fig. 6.** Hyperspectral curves of oilseed rape samples under different Pb concentration stress. Note: (A) and (B) represent the ROI hyperspectral information of oilseed rape leaves and roots, respectively. Besides, (C) and (D) represent the average hyperspectral information of the ROI in oilseed rape leaves and roots under different Pb stress, respectively.

**Table 2**  
SVM models established by spectral data before and after PCA dimensionality reduction.

Data	Oilseed rape leaf			Oilseed rape root		
	NOB	Overall accuracy of training set	Overall accuracy of prediction set	NOB	Overall accuracy of training set	Overall accuracy of prediction set
RAW	411	82.35%	72.50%	411	93.53%	75.00%
SNV	411	95.29%	87.50%	411	95.88%	85.00%
1st Der	410	88.24%	78.75%	410	100%	91.25%
2nd Der	409	86.47%	75.00%	409	98.82%	88.75%
RAW-PCA	43	83.53%	73.75%	26	94.71%	78.75%
SNV-PCA	30	95.88%	88.75%	36	97.06%	88.75%
1st Der-PCA	44	94.12%	80.00%	38	100%	92.50%
2nd Der-PCA	41	87.06%	77.50%	30	98.82%	90.00%

Note: NOB represents the number of bands.

completing the deep network relationship models of D and E. Assuming that the SAE Model of D and E is established in the source domain, and T-SAE algorithm proposed in this study is used to build a single-model transfer network structure of D and F (target domain) (Fig. 4).

As illustrated in Figs. 3 and 4, two T-SAE strategies were implemented and compared. For both cases the weights of the T-SAE network model were initialized with the weights of the SAE models (based on the source domain) and retrained with fine-tuned data from the target domain, whereas the deep feature layer extracted through T-SAE was allowed to be trained from scratch, including initialization with randomly weights. In one case (T-SAE Model 1), the pre-learning networks of SAE Model 1 were kept frozen (Fig. 3), i.e., the weights of the pre-learning network in the primary model were maintained, whereas the depth feature layers of the source network were not preserved. However, in the other case (T-SAE Model 2) the source domain network

parameters (except for the output layer) were all kept frozen. Besides, both T-SAE models (T-SAE Model 1 and T-SAE Model 2) need to be retrained to obtain new depth features.

When the network layers of SAE Model 1 and SAE Model 2 were not the same, the construction of the T-SAE model needed to be translated and expanded. Assuming that the number of SAE Model 1 network layers was  $m$ , and the number of SAE Model 2 network layers was  $n$ , where  $m < n$ . At this time, it was necessary to expand the SAE Model 1 network from the  $m$ -layer to  $n$ -layer without changing the parameters of the depth feature layer of the SAE Model 1 network. Therefore, taking the network extension from the  $m$ -th layer to the  $(m + 1)$ -th layer as an example (Fig. 5), the calculation formula of the  $i$ -th node  $Y_i$  of the  $(m + 1)$ -th layer was as follows:

**Table 3**  
Classification accuracy of SAE deep learning network.

Sample	Number of network layers	Depth feature number	Model scale	Overall accuracy of training set	Overall accuracy of prediction set
Oilseed rape leaf	2	148	411–148	100%	87.50%
	3	108	411–148–108	98.82%	90.00%
	4	66	411–148–108–66	100%	93.75%
	5	38	411–148–108–66–38	100%	88.75%
	6	5	411–148–108–66–38–5	100%	86.25%
Oilseed rape root	2	140	410–140	95.29%	92.50%
	3	92	410–140–92	96.47%	95.00%
	4	51	410–140–92–51	95.88%	93.75%
	5	27	410–140–92–51–27	100%	88.75%
	6	21	410–140–92–51–27–21	95.29%	86.25%
Combination of oilseed rape leaf and root	2	280	821–280	100%	90.00%
	3	160	821–280–160	95.88%	92.50%
	4	126	821–280–160–126	100%	93.75%
	5	55	821–280–160–126–55	100%	90.00%
	6	32	821–280–160–126–55–32	100%	88.75%

Note: Model scale represent the number of nodes in the input layer, hidden layer and output layer. e.g. [411–148–108] denotes a total of 411 neurons in the input layer (i.e., 411 bands of the original input spectrum), and the number of neurons in the network includes two hidden layers are 148 and 108, respectively. Besides, the last hidden layer (108 nodes) is used as the output of SAE network (i.e. input of SVM model).

$$Y_i = \sum_{p=1}^l S_f(\omega_{ij} X_p + b_{ij}) \quad (4)$$

where  $X_p$  is the value of the  $p$ -th node in the  $m$ -th layer,  $\omega_{ij}$  is the network weight from the  $i$ -th node in the  $m$ -th layer to the  $j$ -th node in the  $(m+1)$ -th layer,  $b_{ij}$  is the network bias from the  $i$ -th node in the  $m$ -th layer to the  $j$ -th node in the  $(m+1)$ -th layer, and  $S_f$  denotes the activation function. In addition,  $i = 1, 2, 3, \dots, l$ ;  $j = 1, 2, 3, \dots, l$ . Where  $l$  is the number of the depth feature layer in the SAE Model 1 network.

To ensure that the number of SAE Model 1 network layers is expanded while the output depth feature layer parameters remain unchanged, and the values of  $\omega_{ij}$  and  $b_{ij}$  are as follows:

$$\omega_{ij} = \begin{cases} 0, & i \neq j \\ 1, & i = j \end{cases} \quad (5)$$

$$b_{ij} = 0 \quad (6)$$

Furthermore, the analogy continues until the number of SAE Model 1 network layers is expanded to  $n$  layers. The T-SAE was also executed in Matlab 2014a (The Math Works, Natick, USA) under the framework of the SAE.

## 2.6. Mathematical modeling

Support vector machine (SVM) is a widely used discriminative machine learning algorithm based on statistical learning theory [42,32]. To effectively improve the accuracy of SVM modeling and analysis, the radial basis function (RBF) kernel function [45] and cross-validation search method [36] were adopted in the SVM modeling analysis conducted in this study. Besides, the SVM was used to establish the relationship model between hyperspectral data and environmental Pb concentration categories after data preprocessing (RAW, SNV, 1st Der and 2nd Der) and three data dimensionality reduction processes (PCA, SAE and T-SAE). Further, the support vector machine regression (SVR) algorithm was used to predict lead content in oilseed rape leaves and roots. Among them, the SVM algorithm and the SVR algorithm were the connection bridge from the depth feature layer to the output layer in the SAE and T-SAE deep learning models. Further, the SVM and the SVR was executed in Matlab 2014a (The Math Works, Natick, USA) using a LSSVR toolbox (available at <https://www.esat.kuleuven.be/sista/lssvmlab/>). Finally, the SVR models were evaluating the parameters including coefficient of determination ( $R^2$ ), root mean square error (RMSE), relative percent different (RPD).

## 3. Results and discussion

### 3.1. Sample hyperspectral curve analysis

The original waveband range of the sample collected through the hyperspectral imaging system was 400.68 nm to 1001.61 nm. Owing to the noise generated by the instrument and the environment, this study only deals with hyperspectral data within the range of 480.46 nm to 1001.61 nm. Fig. 6 (A) and (B) show the ROI hyperspectral information of oilseed rape leaves and roots, respectively. The Vis-NIR hyperspectral curves of the leaves and roots were controlled based on their pigment contents, cell structures and biochemical composition [10]. The composition and structure of the leaves and roots are quite different, and thus there is a difference in the curve trend of the leaves and roots.

The ROI average hyperspectral curves of the oilseed rape leaves and roots under five categories of Pb stress concentration (0, 50, 100, 200, 300  $\mu\text{M}$ ) are shown in Fig. 6(C) and (D), respectively. As shown in Fig. 6 (C) and (D), The ROI average spectral curves of the oilseed rape leaves and roots under different Pb stress concentrations show obvious differences. On the one hand, chlorophyll absorbs the blue and red color wavelengths, i.e. approximately 430–450 nm and 640–660 nm [40,28]. In addition, some small weak peaks observed within the range of 750 nm to 900 nm were mainly attributed to the third overtone stretching of the water-related O–H functional group in the oilseed leaves [7]. The absorption region was observed within the range of 900 nm to 980 nm, which corresponded to the third overtone of the C–H functional groups (910 nm) and the second O–H overtone (960 nm) [22]. With the increase of heavy metal Pb stress concentration, the chlorophyll and water content in crop leaves first increased and then decreased, and these changes can be effectively characterized with the hyperspectral information in the visible-near-infrared band [43]. On the other hand, it can be seen that the oilseed rape root samples under CK and 50  $\mu\text{M}$  lead concentration stress have absorption valleys (bottom) in the spectral range of 680–700 nm. While with the increase of lead concentration stress, the oilseed rape root samples under 100, 200 and 300  $\mu\text{M}$  lead concentration stress do not have absorption valleys (bottom) in the 680–700 nm spectral range. The possible reason for this is that the pigments in the vacuolar cells in the mature zone of plant root tips decrease with the increase of heavy metal stress (Feng et al., 2018), and the Chl absorbing light at 690 nm will be partially reabsorbed by the absorption band of the pigment in the body when it is emitted deeper into the root tissue [6]. Besides, the spectral reflectance of the oilseed rape roots within the range of 750–1000 nm is mainly related to its cell structures and biochemical composition [38].

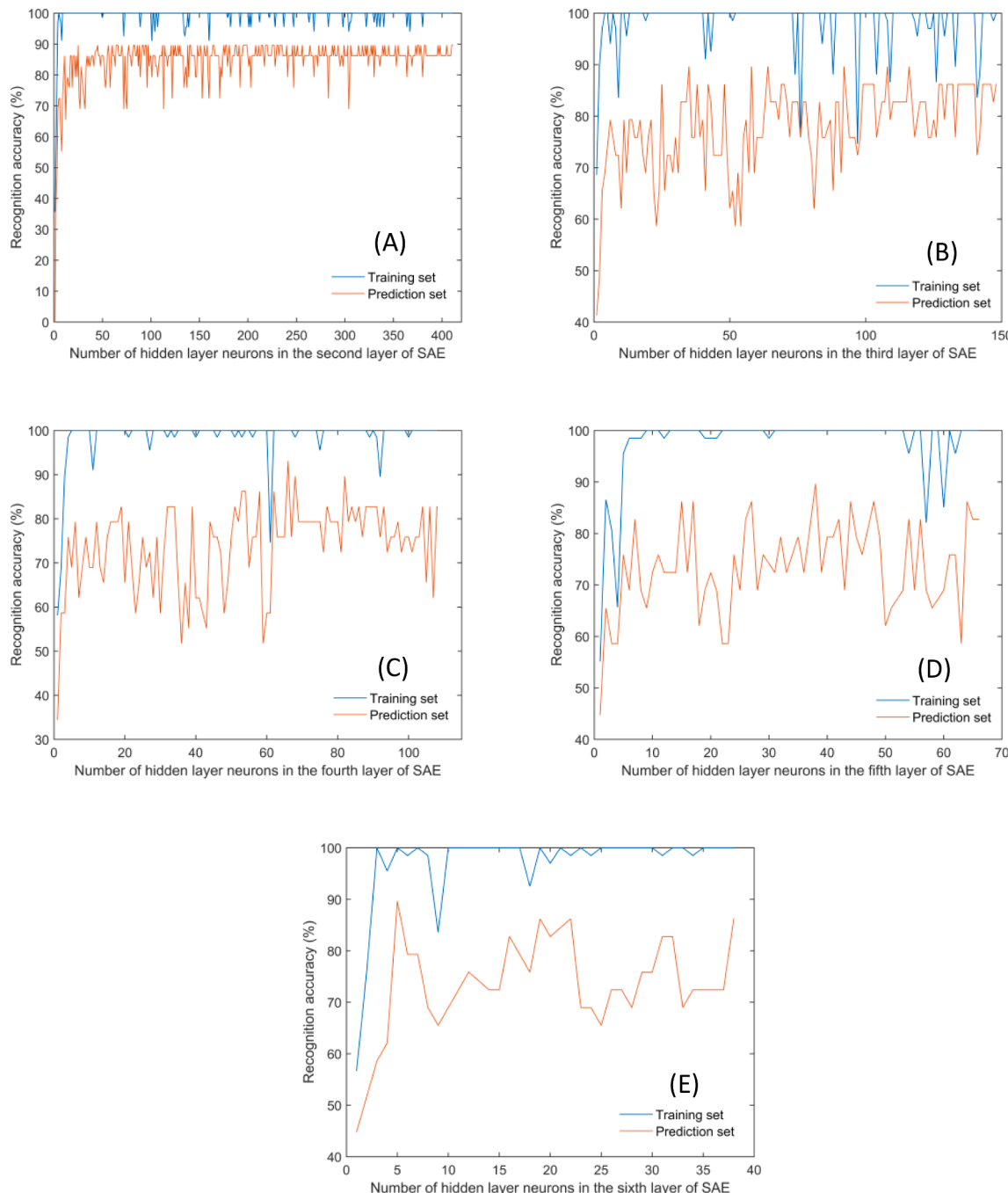


**Fig. 7.** Results of the SAE network based on the oilseed rape leaf data. Note: (A), (B), (C), (D), and (E) represent the node training results of the second, third, fourth, fifth, and sixth SAE network based on oilseed rape leaf data, respectively.

### 3.2. Spectral preprocessing and PCA dimensionality reduction

Three spectral data preprocessing algorithms were used to process the raw spectral data and evaluate the reliability of the modeled data including the standard normalized variable (SNV), first derivative (1st Der) and second derivative (2nd Der). Then, PCA was used to reduce the dimensionality of the spectral data. By comparing the accuracy of the Pb stress concentration classification model established through the spectral data before and after a reduction in the PCA dimensionality reduction, the best pre-processed data were determined for the subsequent research and analysis.

A total of 500 oilseed rape samples (250 oilseed rape leaves and 250 oilseed rape roots) were divided into a training set of 340 samples (170

oilseed rape leaves and 170 oilseed rape roots) and a prediction set of 160 samples (80 oilseed rape leaves and 80 oilseed rape roots). The results of the SVM models for the Pb stress concentration classification established based on the spectral data before and after a reduction in the dimensionality achieved when applying a PCA are shown in Table 2.

It can be seen from Table 2 that the performance of the SVM model for Pb stress concentration classification SVM model established using the preprocessed spectral data is better than the SVM model established by the raw spectral data. In addition, the preprocessing algorithms of the best SVM classification model based on the spectral data of oilseed rape leaves and roots were SNV and 1st Der algorithm, respectively. Besides, PCA can effectively reduce the dimension of the spectral data and improve the performance of the established SVM model. Further, the

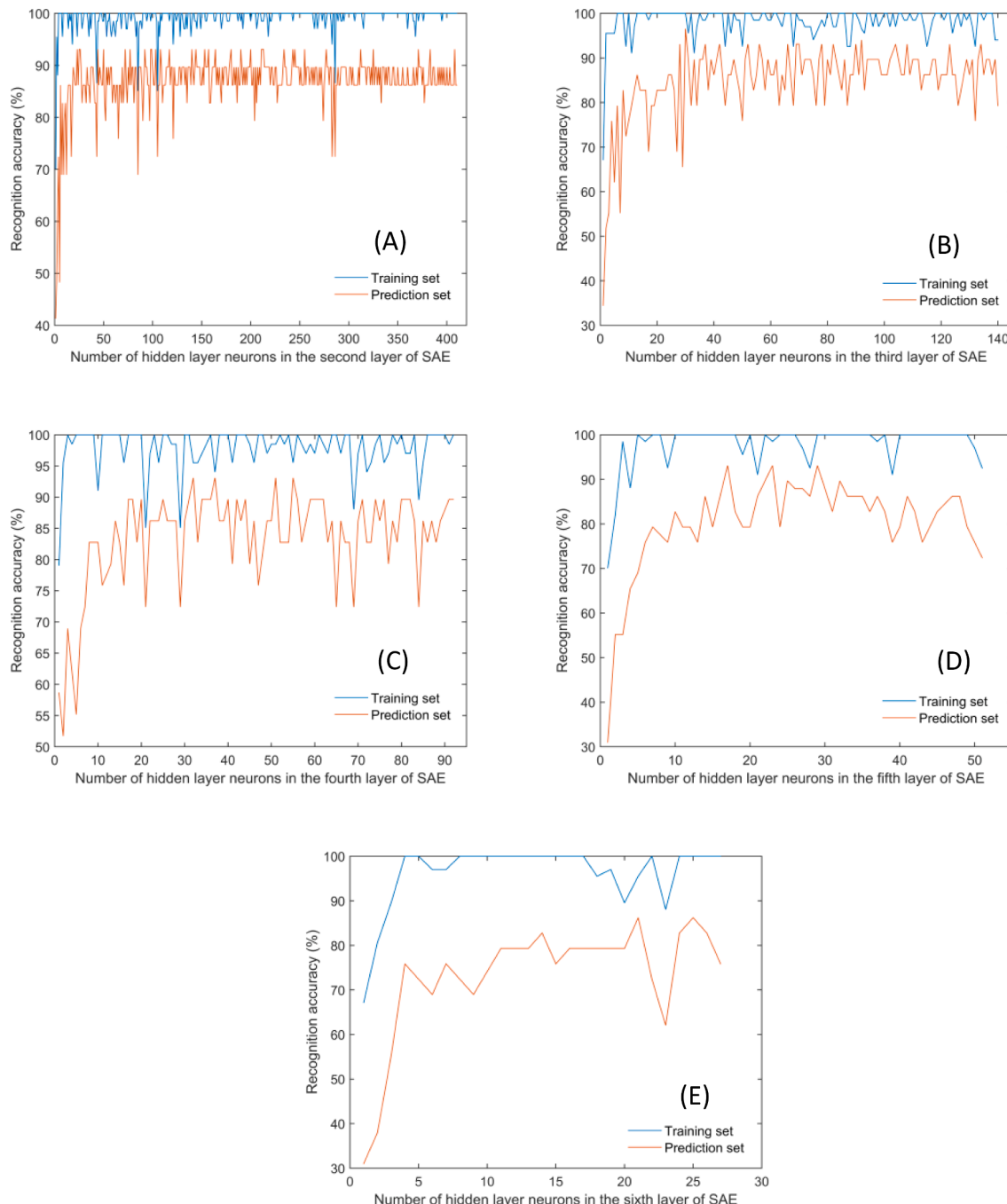


**Fig. 8.** Results of the SAE network based on the oilseed rape root data. Note: (A), (B), (C), (D), and (E) represent the node training results of the second, third, fourth, fifth, and sixth SAE network based on oilseed rape root data, respectively.

prediction accuracy of the SVM classification model established using spectral data from a PCA dimensionality reduction still has room for improvement. To this end, we will try to improve the accuracy of the model through deep learning algorithms.

In this study, the reason that the number of spectral bands is reduced by one after each derivative processing owing to the differential processing of two adjacent bands [25].

### 3.3. SAE depth feature models

In this paper, the spectra of 250 ROIs of oilseed rape leaves spectra after SNV processing and 250 ROIs of oilseed rape roots spectra after 1st Der processing were divided into the training set including 170 oilseed

rape leaves and 170 oilseed rape roots, whereas the remaining 80 oilseed rape leaves and 80 oilseed rape roots were used as the prediction set. In addition, the combined data on oilseed rape leaves and roots (the spectra of 250 ROIs of oilseed rape leaves spectra after SNV processing and 250 ROIs of oilseed rape roots spectra after 1st Der processing) were also be used as the SAE input for the construction of the SAE deep learning network, including a training set of 170 samples and a prediction set of 80 samples. Hence, the oilseed rape leaf and root from the same oilseed rape plant were regarded as samples and the number of bands reached 821 (the original spectral bands of oilseed rape leaf spectral band after SNV processing had 411 bands and those of the oilseed root spectral band after 1st Der processing had 410 bands). In this way, the training set was used to fine-tune the initial parameters of the SAE deep learning

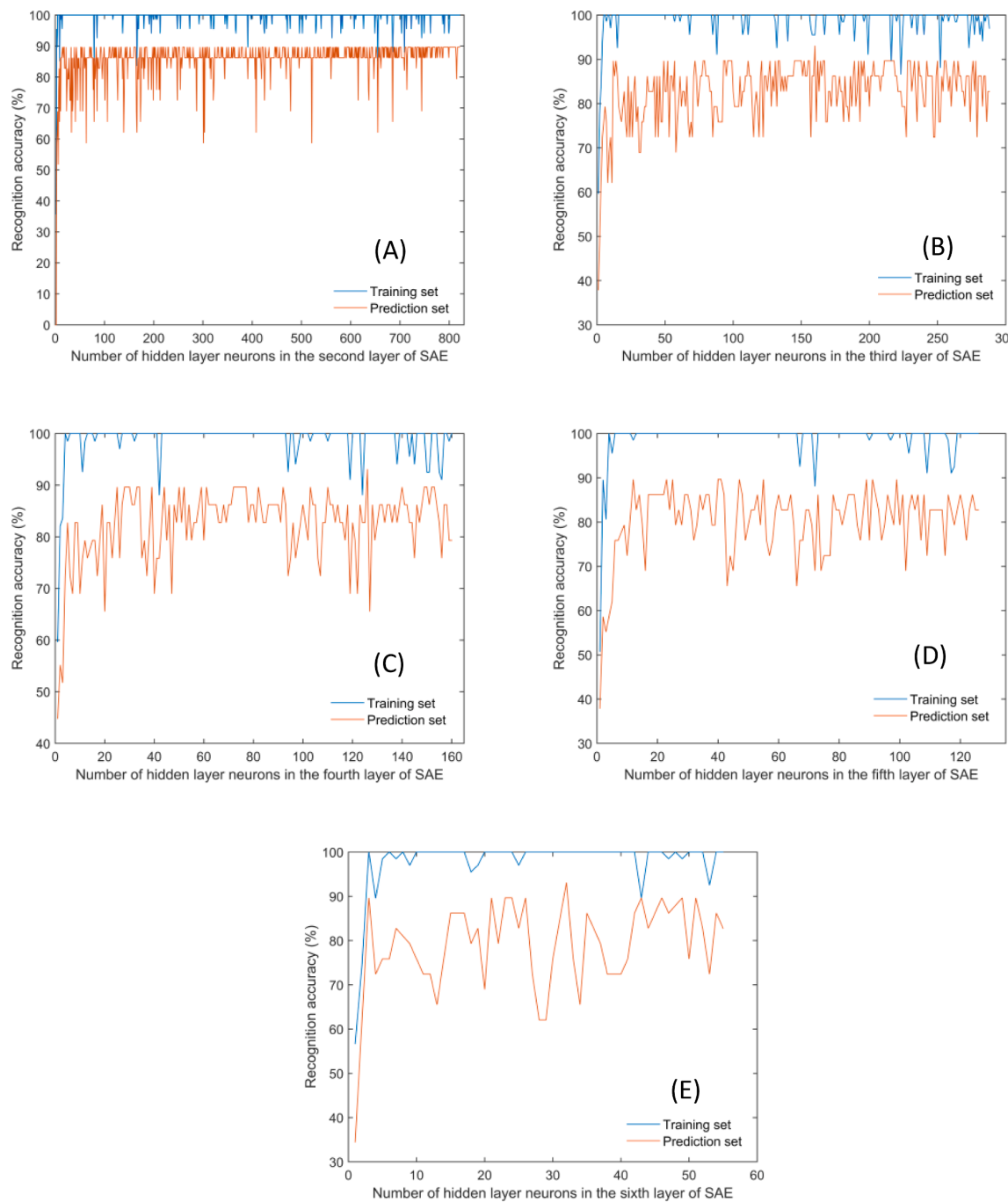


**Fig. 9.** Results of the SAE network based on the combination data of oilseed rape leaf and root. Note: (A), (B), (C), (D), and (E) represent the node training results of the second, third, fourth, fifth, and sixth SAE network based on the combination data of oilseed rape leaf and root, respectively.

model using the gradient descent algorithm, and the prediction set was used to evaluate the performance of the SAE deep learning model.

In addition, the best network nodes and classification accuracy of SAE deep learning network based on the oilseed rape leaf data set, oilseed rape root data set, and the combined data of oilseed rape leaf and root are shown in Table 3. Furthermore, the results of the SAE network based on the oilseed rape leaf data set, oilseed rape root data set, and the combined data of oilseed rape leaf and root using the gradient descent method are shown in Figs. 7, 8 and 9, respectively. Comparing Figs. 7, 8 and 9 and Table 3, it can be seen that as the number of SAE network layers increases, the accuracy of the Pb stress concentration classification models established based on the oilseed rape leaf data set, oilseed rape root data set, and the combined data of oilseed rape leaf and root all

show increases followed by decreases. The model scales of the best SAE depth models established based on the oilseed rape leaf data set, oilseed rape root data set, and the combined data of oilseed rape leaf and root data set were 411–148–108–66, 410–140–92 and 821–280–160–126, respectively. Additionally, the best SAE depth models' accuracy of the prediction set based on the oilseed rape leaf data set, oilseed rape root data set, and the combined data of oilseed rape leaf and root data set were 93.75%, 95.00% and 93.75%, respectively. The performance of the SAE model established based on the combined data of oilseed rape leaf and root data set was the same as that of oilseed rape leaf and lower than that of oilseed rape root. One possible reason for this is the fact that the best SAE model layers of the oilseed rape leaf and root were not the same, of which the best SAE network layers of the oilseed rape leaf data

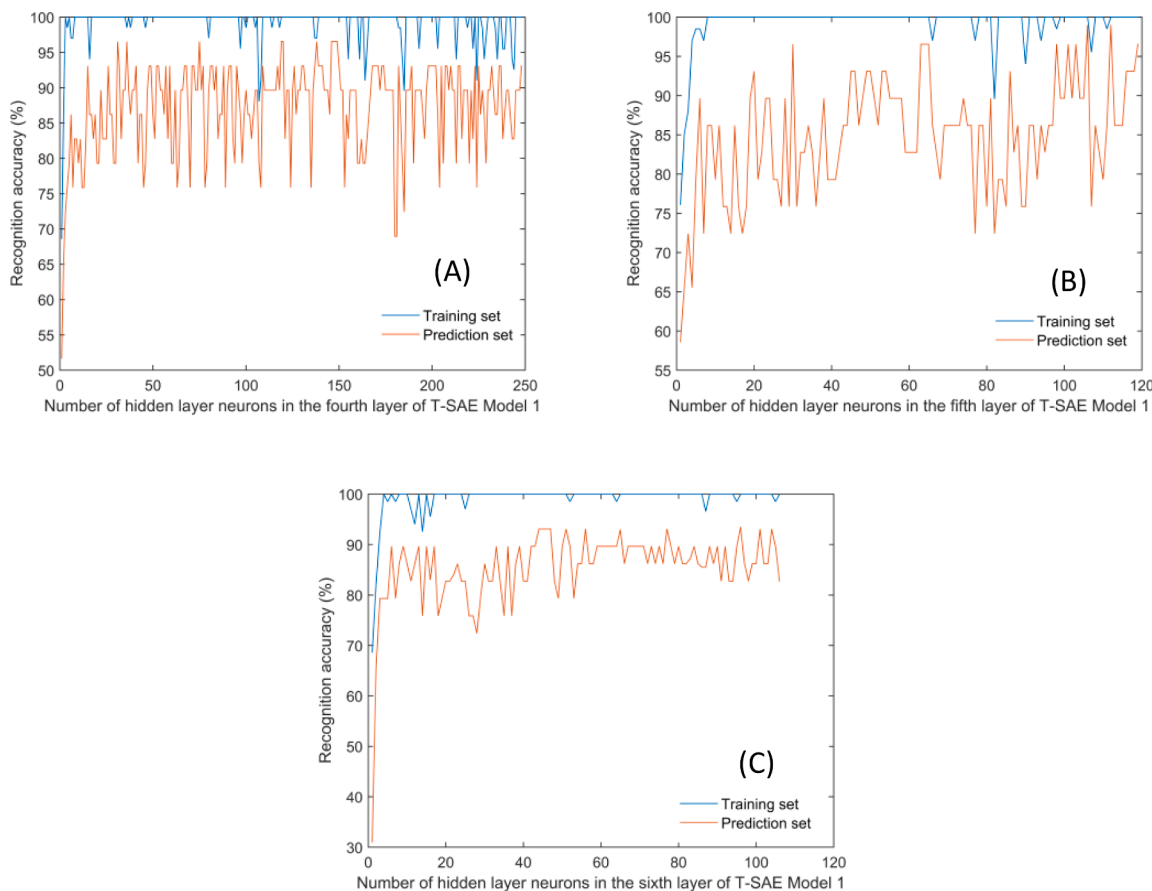


**Fig. 10.** Results of the dual-model T-SAE Model 1 network. Note: (A), (B), and (C) represent the node training results of the fourth, fifth, and sixth T-SAE Model 1 network, respectively.

set and oilseed rape root data set were 4 and 3, respectively. For this reason, the fusion processing of oilseed rape leaf and root data from the input layer failed to achieve the highest classification accuracy.

#### 3.4. T-SAE depth feature models

Hence, the best SAE models of the Pb stress concentration classification established based on oilseed rape leaf data and oilseed rape root data were regarded as SAE Model 1 and SAE Model 2, respectively. Based on the established SAE Model 1 and SAE Model 2 of the optimal Pb stress concentration classification, T-SAE Model 1 and T-SAE Model 2 were constructed through transfer learning methods, respectively.

As shown in Figs. 10, 11 and Table 4, the model scales of the best T-SAE Model 1 and T-SAE Model 2 were 821–288–248–119–106 and 821–288–200–158–96, respectively. As an aside, the overall accuracy rates of the training and prediction sets for the best T-SAE Model 1 were 100% and 98.75%, respectively. Furthermore, the overall accuracy rates of the training set and prediction set in the best T-SAE Model 2 were 100% and 97.50%, respectively. The results showed that the performance of the T-SAE network model established through transfer learning was better than the SAE deep learning network. Clearly, the performance of the established best T-SAE Model 1 was better than that of T-SAE Model 2. This results showed that the classification accuracy of the Pb stress concentration in T-SAE Model 1 established through dual-model T-SAE transfer learning without a depth feature layer was higher than that of T-SAE Model 2 established through transfer learning with a depth feature layer.

Furthermore, the best SAE models of the Pb stress concentration classification established based on oilseed rape plant (leaf and root) data was regarded as SAE Model. Based on the established SAE Model of the

optimal Pb stress concentration classification, T-SAE Model 1 and T-SAE Model 2 prediction models of lead content in oilseed rape plants (leaf and root) were constructed by transfer learning method (Table 5), respectively. From the results in Table 5 and Fig. 12, the performance of the established T-SAE Model 1 model for the prediction of lead content in oilseed rape plants (leaf and root) was better than that of T-SAE Model 2. Among them, the model scale,  $R_p^2$ , RMSEP and RPD in the best T-SAE Model 1 of oilseed rape leaves were 411–148–108–60, 0.9215, 0.0302 mg/kg and 3.119, respectively. Moreover, the model scale,  $R_p^2$ , RMSEP and RPD in the best T-SAE Model 1 of oilseed rape roots were 410–140–91–56, 0.9349, 0.0278 mg/kg and 3.264, respectively. The results further showed that the performance of the Pb content prediction model in T-SAE model 1 established by single-model T-SAE transfer learning without deep feature layers was higher than that of T-SAE model 2 established by transfer learning with deep feature layers.

#### 4. Conclusion

This paper demonstrated the feasibility of using hyperspectral technology combined with a T-SAE deep transfer learning algorithm to classify the Pb stress concentration and detect the Pb concentration of oilseed rape plants. The results of T-SAE Model 1 (without a depth feature layer) and T-SAE Model 2 (including a depth feature layer) data will encourage more studies on deep transfer learning algorithms and their application to actual detection work. To obtain a more effective and accurate model, in future research, we will apply the deep transfer learning methods based on hyperspectral technology to the study of other heavy metal stresses, crop varieties, locations and optimization algorithms to reflect other agronomic differences.

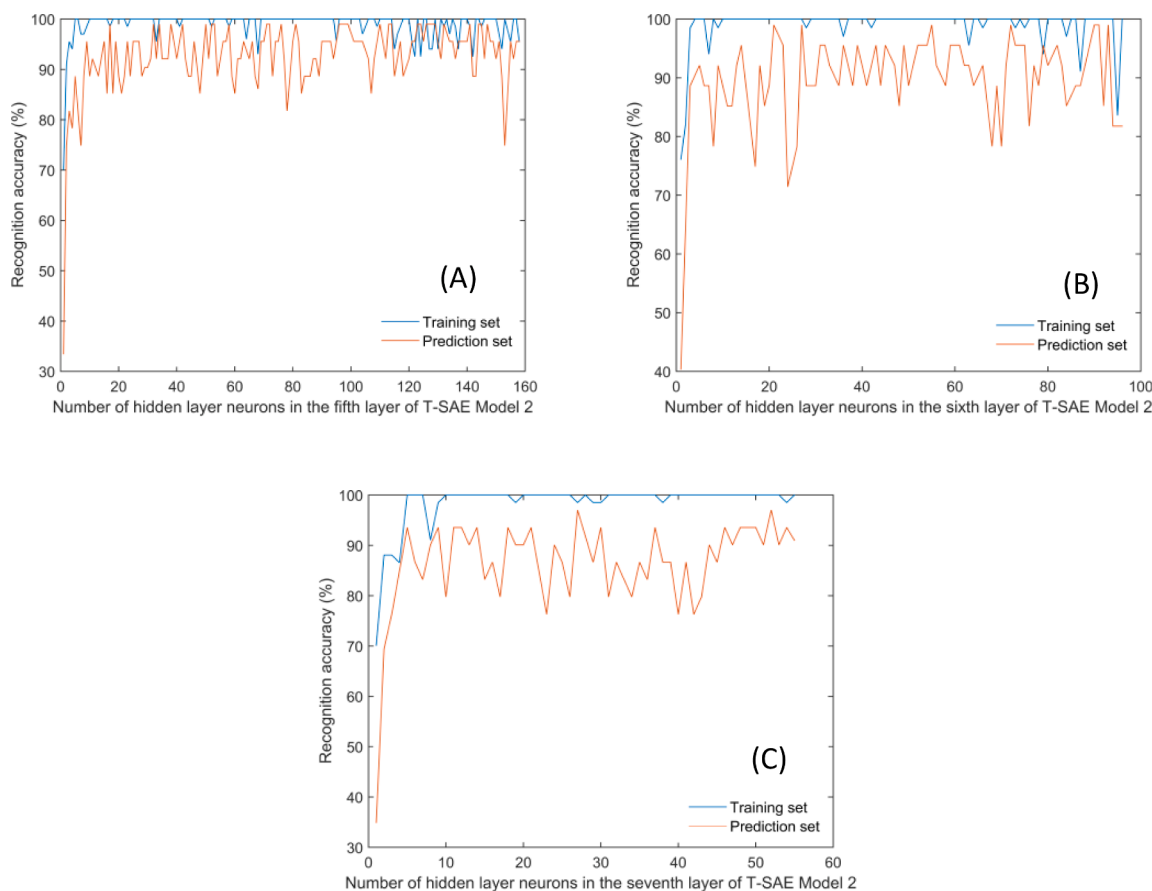


**Fig. 11.** Results of the dual-model T-SAE Model 2 network. Note: (A), (B), and (C) represent the node training results of the fifth, sixth, and seventh T-SAE Model 2 network, respectively.

**Table 4**  
Classification results of T-SAE deep learning network.

Model	Number of network layers	Depth feature number	Model scale	Overall accuracy of training set	Overall accuracy of prediction set
T-SAE Model 1	4	119	821–288–248–119	100%	96.25%
	5	106	821–288–248–119–106	100%	98.75%
	6	56	821–288–248–119–106–56	100%	93.75%
T-SAE Model 2	5	96	821–288–200–158–96	100%	97.50%
	6	55	821–288–200–158–96–55	100%	96.25%
	7	27	821–288–200–158–96–55–27	100%	95.00%

**Table 5**  
Quantitative detection results of T-SAE deep learning network.

Model	Sample	Model scale	Training set		Prediction set		
			R <sup>2</sup> <sub>c</sub>	RMSEC (mg/kg)	R <sup>2</sup> <sub>p</sub>	RMSEP (mg/kg)	RPD
T-SAE Model 1	Oilseed rape leaf	411–148–108–60	0.9640	0.0195	0.9215	0.0302	3.119
		411–148–108–60–41	0.9530	0.0207	0.9063	0.0435	3.087
		411–148–108–60–41–27	0.9422	0.0261	0.8977	0.0449	2.964
	Oilseed rape root	410–140–91	0.9609	0.0198	0.9186	0.0337	3.107
		410–140–91–56	0.9711	0.0160	0.9349	0.0278	3.264
		410–140–91–56–33	0.9571	0.0201	0.9034	0.0439	3.029
T-SAE Model 2	Oilseed rape leaf	411–148–108–66–59	0.9602	0.0200	0.9197	0.0326	3.112
		411–148–108–66–59–43	0.9514	0.0219	0.9094	0.0431	3.096
		411–148–108–66–59–43–30	0.9444	0.0257	0.8951	0.0452	2.959
	Oilseed rape root	410–140–92–87	0.9688	0.0182	0.9299	0.0294	3.188
		410–140–92–87–61	0.9545	0.0211	0.9141	0.0347	3.101
		410–140–92–87–61–39	0.9513	0.0220	0.9020	0.0440	3.005

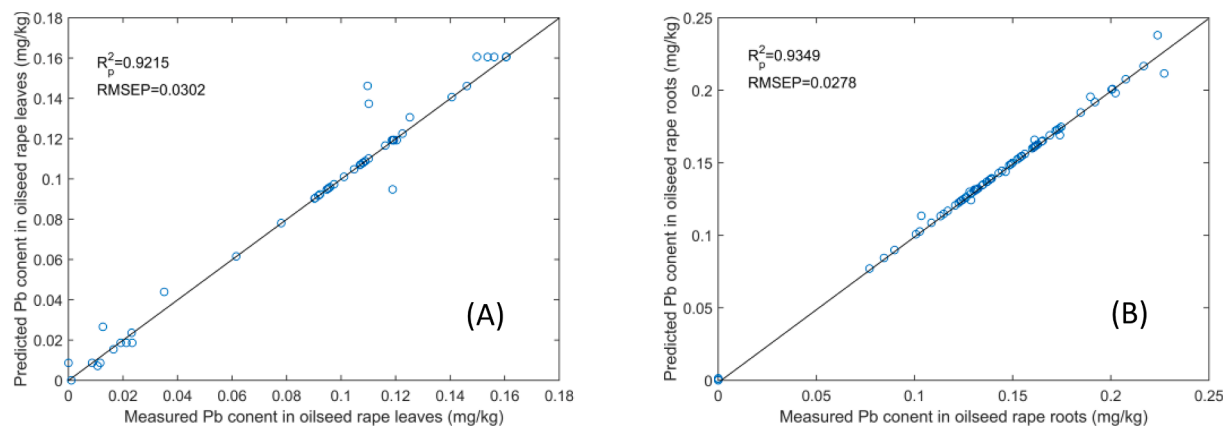


**Fig. 12.** Results of the best T-SAE model for Pb content prediction. Note: (A) and (B) represent the best results for the prediction of Pb content of oilseed rape leaves and roots using the T-SAE models, respectively.

#### Declaration of Competing Interest

The authors declare that they have no known competing financial interests or personal relationships that could have appeared to influence the work reported in this paper.

#### Data availability

Data will be made available on request.

#### Acknowledgments

This work is partially supported by National natural science funds projects (32201653, 31971788), Project funded by China Postdoctoral Science Foundation (2021M701479), the Priority Academic Program Development of Jiangsu Higher Education Institutions (PAPD-2018-87), Research project of Jiangsu University undergraduates (Y20A058).

#### References

- [1] S. Anwar, H. Lei, J. Kuai, S. Khan, S. Fahad, G. Zhou, Soaking seeds of winter rapeseed with quinalfop-p-ethyl alters plant growth and improves yield in a rice-rapeseed cropping system, *Field Crop Res* 208 (2017) 11–17, <https://doi.org/10.1016/j.fcr.2017.04.001>.
- [2] E. Bassi, R. Facoetti, M. Ferloni, A. Pastorino, A. Bianchi, G. Fedrizzi, I. Bertoletti, A. Andreotti, Lead contamination in tissues of large avian scavengers in south-central Europe, *Sci. Total Environ.* 778 (2021) 146130.
- [3] B. Becker, D. Lusch, J. Qi, Identifying optimal spectral bands from in situ measurements of great lakes coastal wetlands using second-derivative analysis, *Remote Sens. Environ.* 97 (2) (2005) 238–248, <https://doi.org/10.1016/j.rse.2005.04.020>.
- [4] Y. Cao, J. Sun, K. Yao, M. Xu, N. Tang, X. Zhou, Nondestructive detection of lead content in oilseed rape leaves based on MRF-HHO-SVR and hyperspectral technology, *J. Food Process Eng* e13793 (2021), <https://doi.org/10.1111/jfpe.13793>.
- [5] R. Chakraborty, G. Kerestturi, R. Pullanagari, P. Durance, S. Ashraf, C. Anderson, Mineral prospecting from biogeochemical and geological information using hyperspectral remote sensing—Feasibility and challenges, *Geochem. Explor.* 232 (2022), 106900, <https://doi.org/10.1016/j.gexplo.2021.106900>.
- [6] J. Cherif, N. Derbel, M. Nakach, H. Bergmann, F. Jemal, Z. Lakhdar, Analysis of in vivo chlorophyll fluorescence spectra to monitor physiological state of tomato plants growing under zinc stress, *J. Photochem. Photobiol. B Biol.* 101 (3) (2021) 332–339, <https://doi.org/10.1016/j.jphotobiol.2010.08.005>.
- [7] M. Corti, P. Marino Gallina, D. Cavalli, G. Cabassi, Hyperspectral imaging of spinach canopy under combined water and nitrogen stress to estimate biomass, water, and nitrogen content, *Biosyst. Eng.* 158 (2017) 38–50, <https://doi.org/10.1016/j.biosystemseng.2017.03.006>.
- [8] C. Cui, T. Fearn, Modern practical convolutional neural networks for multivariate regression: applications to nir calibration, *Chemom. Intel. Lab. Syst.* 182 (2018) 9–20, <https://doi.org/10.1016/j.chemolab.2018.07.008>.
- [9] A. Fazari, O. Pellicer-Valero, J. Gomez-Sanchs, B. Bernardi, J. Blasco, Application of deep convolutional neural networks for the detection of anthracnose in olives using vis/nir hyperspectral images, *Comput. Electron. Agric.* 187 (2021), 106252, <https://doi.org/10.1016/j.compag.2021.106252>.
- [10] X. Feng, H. Chen, Y. Chen, C. Zhang, Y. He, Rapid detection of cadmium and its distribution in miscanthus sacchariflorus based on visible and near-infrared hyperspectral imaging, *Sci. Total Environ.* 659 (2019) 1021–1031, <https://doi.org/10.1016/j.scitotenv.2018.12.458>.
- [11] Z. Gumus, M. Soylak, Metal organic frameworks as nanomaterials for analysis of toxic metals in food and environmental applications, *TrAC Trends Anal. Chem.* 143 (2021), 116417, <https://doi.org/10.1016/j.trac.2021.116417>.
- [12] Y. Jeong, J. Yu, L. Wang, K. Lee, Bulk scanning method of a heavy metal concentration in tailings of a gold mine using swir hyperspectral imaging system, *Int. J. Appl. Earth Observ. Geoinform.* 102 (2021), 102382, <https://doi.org/10.1016/j.jag.2021.102382>.
- [13] C. Ji, Y. Zhai, T. Zhang, X. Shen, Y. Bai, J. Hong, Carbon, energy and water footprints analysis of rapeseed oil production: a case study in china, *J. Environ. Manage.* 287 (2021), 112359, <https://doi.org/10.1016/j.jenvman.2021.112359>.
- [14] I. Jolliffe, A 50-year personal journey through time with principal component analysis, *J. Multivar. Anal.* 104820 (2021), <https://doi.org/10.1016/j.jmva.2021.104820>.
- [15] C. Liu, Risk prediction of digital transformation of manufacturing supply chain based on principal component analysis and backpropagation artificial neural network, *Alex. Eng. J.* 61 (1) (2022) 775–784, <https://doi.org/10.1016/j.aej.2021.06.010>.
- [16] P. Mishra, G. Polder, A. Gowen, D. Rutledge, G. Roger, Utilising variable sorting for normalisation to correct illumination effects in close-range spectral images of potato plants, *BiosystemsEngineering* 197 (2020) 318–323, <https://doi.org/10.1016/j.biosystemseng.2020.07.010>.
- [17] P. Mishra, Deep calibration transfer: transferring deep learning models between infrared spectroscopy instruments, *Infrared Phys. Technol.* 117 (2021), 103863, <https://doi.org/10.1016/j.infrared.2021.103863>.
- [18] C. Niu, K. Tan, X. Jia, X. Wang, Deep learning based regression for optically inactive inland water quality parameter estimation using airborne hyperspectral imagery, *Environ. Pollut.* 286 (2021), 117534, <https://doi.org/10.1016/j.envpol.2021.117534>.
- [19] J. Padarian, B. Minasny, A. Mcbratney, Transfer learning to localise a continental soil vis-nir calibration model, *Geoderma* 340 (2019) 279–288, <https://doi.org/10.1016/j.geoderma.2019.01.009>.
- [20] G. Qin, Z. Niu, J. Yu, Z. Li, P. Xiang, Soil heavy metal pollution and food safety in china: effects, sources and removing technology, *Chemosphere* 267 (2021), 129205, <https://doi.org/10.1016/j.chemosphere.2020.129205>.
- [21] C. Sarah, F. Luca, S. Lorenzo, B. Luciano, C. Jacopo, N. Enrico, B. Stefania, Use of a portable near-infrared tool for rapid on-site inspection of freezing and hydrogen peroxide treatment of cuttlefish (*Sepia officinalis*), *Food Control* 132 (2022), 108524, <https://doi.org/10.1016/j.foodcont.2021.108524>.
- [22] T. Shi, J. Ma, Y. Zhang, C. Liu, L. Zhao, Status of lead accumulation in agricultural soils across china (1979–2016), *Environ. Int.* 129 (2019) 35–41, <https://doi.org/10.1016/j.envint.2019.05.025>.
- [23] H. Suk, S. Lee, D. Shen, Latent feature representation with stacked auto-encoder for AD/MCI diagnosis, *Brain Struct. Funct.* 220 (2) (2015) 841–859, <https://doi.org/10.1007/s00429-013-0687-3>.
- [24] J. Sun, X. Zhou, Y. Hu, X. Wu, X. Zhang, P. Wang, Visualizing distribution of moisture content in tea leaves using optimization algorithms and NIR hyperspectral imaging, *Comput. Electron. Agric.* 160 (2019) 153–159, <https://doi.org/10.1016/j.compag.2019.03.004>.
- [25] K. Tan, H. Wang, L. Chen, Q. Du, P. Du, C. Pan, Estimation of the spatial distribution of heavy metal in agricultural soils using airborne hyperspectral imaging and random forest, *J. Hazard. Mater.* 382 (2020), 120987, <https://doi.org/10.1016/j.jhazmat.2019.120987>.
- [26] S. Ustin, A. Gitelson, S. Jacquemoud, M. Schaepman, G. Asner, J. Gamon, et al., Retrieval of foliar information about plant pigment systems from high resolution spectroscopy, *Remote Sens. Environ.* 113 (1) (2009) S67–S77, <https://doi.org/10.1016/j.rse.2008.10.019>.

- [29] W. Wambugu, Y. Chen, Z. Xiao, K. Yan, M. Wei, X. Liu, J. Li, Hyperspectral image classification on insufficient-sample and feature learning using deep neural networks: a review, *Int. J. Appl. Earth Obs. Geoinf.* 105 (2021), 102603, <https://doi.org/10.1016/j.jag.2021.102603>.
- [30] Y. Wang, H. Ma, J. Wang, L. Liu, M. Pietikäinen, Z. Zhang, X. Chen, Hyperspectral monitor of soil chromium contaminant based on deep learning network model in the eastern junggar coalfield, *Spectrochim. Acta A Mol. Biomol. Spectrosc.* 257 (2021), 119739, <https://doi.org/10.1016/j.saa.2021.119739>.
- [31] X. Wang, F. Zhang, H. Kung, V. Johnson, New methods for improving the remote sensing estimation of soil organic matter content (SOMC) in the ebinur lake wetland national nature reserve (ELWNNR) in northwest china, *Remote Sens. Environ.* 218 (2018) 104–118, <https://doi.org/10.1016/j.rse.2018.09.020>.
- [32] K. Yao, J. Sun, C. Chen, M. Xu, X. Zhou, Y. Cao, Y. Tian, Non-destructive detection of egg qualities based on hyperspectral imaging, *J. Food Eng.* 325 (2022), 111024, <https://doi.org/10.1016/j.jfoodeng.2022.111024>.
- [33] K. Yu, S. Fang, Y. Zhao, Heavy metal hg stress detection in tobacco plant using hyperspectral sensing and data-driven machine learning methods, *Spectrochim. Acta A Mol. Biomol. Spectrosc.* 245 (2020), 118917, <https://doi.org/10.1016/j.saa.2020.118917>.
- [35] X. Yu, H. Lu, D. Wu, Development of deep learning method for predicting firmness and soluble solid content of postharvest korla fragrant pear using vis/nir hyperspectral reflectance imaging, *Postharvest Biol. Technol.* 141 (2018) 39–49, <https://doi.org/10.1016/j.postharvbio.2018.02.013>.
- [36] X. Zhang, J. Sun, P. Li, F. Zeng, H. Wang, Hyperspectral detection of salted sea cucumber adulteration using different spectral preprocessing techniques and SVM method, *LWT-Food Sci. Technol.* 152 (5) (2021), 112295, <https://doi.org/10.1016/j.lwt.2021.112295>.
- [37] F. Zhao, Y. Ma, Y. Zhu, T. Zhong, S. McGrath, Soil contamination in china: current status and mitigation strategies, *Environ. Sci. Tech.* 49 (2) (2015) 750–759, <https://doi.org/10.1021/es5047099>.
- [38] Q. Zheng, Y. Zhao, J. Wang, T. Liu, B. Zhang, M. Gong, et al., Spectrum-effect relationships between uplc fingerprints and bioactivities of crude secondary roots of aconitum carmichaelii debeaux (Fuzi) and its three processed products on mitochondrial growth coupled with canonical correlation analysis, *J. Ethnopharmacol.* 153 (3) (2014) 615–623, <https://doi.org/10.1016/j.jep.2014.03.011>.
- [40] X. Zhou, J. Sun, Y. Tian, B. Lu, Y. Hang, Q. Chen, Hyperspectral technique combined with deep learning algorithm for detection of compound heavy metals in lettuce, *Food Chem.* 321 (2020), 126503, <https://doi.org/10.1016/j.foodchem.2020.126503>.
- [41] X. Zhou, J. Sun, Y. Tian, B. Lu, Y. Hang, Q. Chen, Development of deep learning method for lead content prediction of lettuce leaf using hyperspectral images, *Int. J. Remote Sens.* 41 (6) (2019) 2263–2276, <https://doi.org/10.1080/01431161.2019.1685721>.
- [42] X. Zhou, J. Sun, Y. Zhang, Y. Tian, K. Yao, M. Xu, Visualization of heavy metal cadmium in lettuce leaves based on wavelet support vector machine regression model and visible-near infrared hyperspectral imaging, *J. Food Process Eng* 44 (12) (2021) e13897.
- [43] X. Zhou, J. Sun, Y. Tian, K. Yao, M. Xu, Detection of heavy metal lead in lettuce leaves based on fluorescence hyperspectral technology combined with deep learning algorithm, *Spectrochim. Acta A Mol. Biomol. Spectrosc.* 266 (2022), 120460, <https://doi.org/10.1016/j.saa.2021.120460>.
- [45] H. Zhu, L. Yang, J. Fei, L. Zhao, Z. Han, Recognition of carrot appearance quality based on deep feature and support vector machine, *Comput. Electron. Agric.* 186 (2021), 106185, <https://doi.org/10.1016/j.compag.2021.106185>.